

Research Article

Computational analysis of charge transfer and optoelectronic properties in triphenylamine-based molecules for high-efficiency organic solar cells

Mohammed Elkabous, Mohammed Ouachekradi, Yasser Karzazi*

Laboratory of Applied Chemistry and Environment, Faculty of Sciences, University Mohammed I, BP 4808, Oujda 60046, Morocco

ARTICLE INFO

Keywords:

 Organics solar cells
 DFT
 Molecular dynamics
 Charge transfer
 Triphenylamine

ABSTRACT

The global energy landscape is undergoing a profound transformation, driven by the urgent need to address environmental concerns and energy security. In recent years, alternative solar energy technologies have attracted increasing interest and investment, and organic solar cells (OSCs) have emerged as promising alternatives to traditional silicon-based solar cells. In this study, a series of four Mi donor materials ($i = 1-4$) incorporating triphenylamine with donor-acceptor-acceptor (D-A-A) configurations was developed. These materials were designed by modifying the acceptor portion of the reference molecule TPA-R by incorporating four different fragments containing sulfur heterocycles, selenophene, and thiadiazole. The electronic and optical properties of small electron donor materials (SEDMs) were explored through theoretical analysis using density functional theory (DFT) simulations at the B3LYP/def2-SVP level of theory to optimize the geometrical structures and the TD-CAM-B3LYP/6-31G(d,p) approach to predict the excitation behavior. The theoretical results were then compared with experimental data, revealing a high degree of agreement. All the designed compounds, M1–M4, showed prominent and broad absorption peaks in the visible spectra, ranging from 595 to 726 nm, with comparatively smaller energy gaps (E_g) than the reference TPA-R. Excited-state analysis revealed that all the designed molecules exhibited a significantly high electron-hole transfer rate from the D moiety to the second A2 acceptor, indicating that modification of the first acceptor improves the charge transfer properties. To fully understand how the small donor molecules interact with the C70 acceptor, molecular dynamics (MD) was performed.

1. Introduction

Organic solar cells (OSCs) have garnered significant attention owing to their inexpensive manufacturing process and the wide range of functionalities offered by organic materials [1,2]. OSCs are not intended to replace existing technologies but rather to complement them by adapting to market needs. However, OSCs present certain drawbacks that limit their widespread use in the field of solar energy, such as low photoconversion efficiency and limited lifetime compared with inorganic cells [3,4]. These drawbacks necessitate improvements in achieving economic reliability and large-scale industrial development. Accordingly, research efforts have actively focused on enhancing these aspects and streamlining material implementation. Over the past decade, conversion efficiencies have doubled and significant progress has been made, particularly regarding material stability. The performance of an OSC is contingent on the active layer architecture, which comprises a judiciously designed blend of electron acceptor and electron donor materials. Electron acceptors can be divided into two main categories. The first includes fullerene derivatives such as [6,6]-phenyl-C₆₀-butyric acid methyl ester

(PCBM), specifically PC61BM [5] and PC71BM [6]. The second consists of non-fullerene alternatives such as ITIC [7], Y6 [8], and the polymer PY-IT [9]. Semiconducting polymers [9,10] and small-molecule compounds [11,12] have been extensively explored as donors. This donor-acceptor (D-A) blend is strategically sandwiched between two electrodes to form a bulk heterojunction (BHJ) structure. To achieve optimal performance in OSCs, it is essential to use donors with excess electrons and acceptors that lack electrons. Polymer- and small-molecule-based OSCs have been intensively studied in recent years [13,14]. In addition to aiming for maximum performance efficiency with polymer donor materials, there has been significant emphasis on designing small molecule donors. The conduction in these materials is ensured by the presence of the π electron system or delocalized electrons throughout the macromolecule skeleton, imparting unique properties compared to saturated systems [15]. Consequently, electron delocalization induces rigidity and enhances the charge transport properties [16], thereby potentially improving the overall efficiency and stability of OSCs. Owing to their unique properties, small-molecule donors [17–19] have generated significant interest in next-generation OSCs [20]. Small molecules offer distinct ad-

* Corresponding author.

E-mail address: y.karzazi@ump.ac.ma (Y. Karzazi).
<https://doi.org/10.1016/j.chphma.2025.08.003>

Received 10 June 2025; Received in revised form 16 July 2025; Accepted 3 August 2025

Available online 3 September 2025

2772-5715/© 2025 The Authors. Publishing Services by Elsevier B.V. on behalf of KeAi Communications Co. Ltd. This is an open access article under the CC BY-NC-ND license (<http://creativecommons.org/licenses/by-nc-nd/4.0/>)

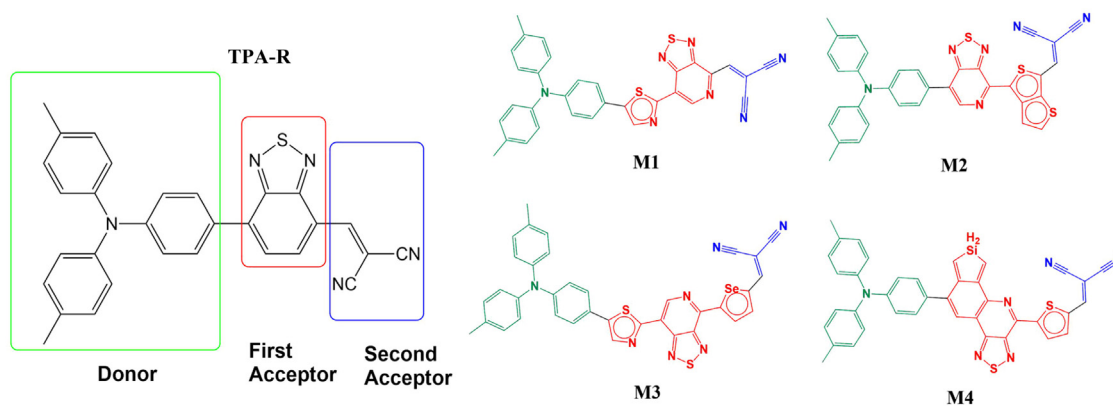


Fig. 1. Structures of the reference molecule TPA-R and the designed molecules M1–M4.

vantages, including increased hole mobility [21], optimized structural morphology [22], higher open-circuit voltage (V_{OC}) values [21], convenient and cost-effective manufacturing processes, exceptional synthetic repeatability leading to high purity, and well-defined low molar mass [23]. This precise molecular structure translates into specific morphologies within the OSC film, promoting the efficient movement of charge carriers—electrons and holes [24].

The design concept known as the “push-pull” strategy (D-A configuration), with electronic imbalances created by push and pull units, enables efficient charge transfer and exciton separation in optoelectronic devices [25,26]. Tailoring their molecular structure allows for the optimization of optoelectronic properties, adjustment of the highest occupied molecular orbital (HOMO)/unoccupied molecular orbital (LUMO) energy levels, and enhancement of charge transport through extended conjugated bridges [27–29]. Overcoming the challenges associated with developing new donor small molecules involves the implementation of favorable structural and molecular modifications within the d-A small molecule process. This strategy forms the basis for constructing small molecule donors in a donor-acceptor-acceptor (D-A-A) configuration [30,31], allowing for the downward adjustment of the energy levels. Furthermore, the photon absorption and charge transfer (exciton) mobility can be enhanced by modifying one or more parts, either through substitution or replacement. Leveraging quantum chemistry in theoretical studies provides the most effective means of predicting the impact of these modifications, offering a powerful approach for predicting the performance of molecules in OSCs. This has led to cost-effective synthesis, improved efficiency, tailored molecular design, and accelerated discovery of novel materials [32,33]. In recent years, the design and exploration of donor materials comprising both polymeric and small-molecule compounds have relied heavily on density functional theory (DFT) and time-dependent DFT (TD-DFT) methodologies [34–38]. These computational approaches have proven invaluable in elucidating structure-property relationships, predicting optoelectronic characteristics, and guiding the rational design of donor materials with tailored properties for organic photovoltaic applications.

In this study, a series of small electron donor materials (SEDMs), denoted as M1, M2, M3, and M4, along with the reference molecule TPA-R based on a triphenylamine (TPA) core, were theoretically developed to predict their performance for OSC applications. The designed molecules M_i ($i = 1-4$) were obtained through systematic modifications of the reference compound TPA-R [39] given its distinctive electron-donating effectiveness, exceptional capacity for electron-hole transfer, and redshift of maximum absorption. These materials were described as having a π -conjugated d-A-A configuration. To accomplish this, we modified the first acceptor unit of the reference molecule using fragments such as 7-(thiazol-2-yl)-[1,2,5]thiadiazolo[3,4-c]pyridine (M1), 7-(thieno[3,4-b]thiophen-3-yl)-[1,2,5]thiadiazolo[3,4-c]pyridine (M2), 4-(selenophen-2-yl)-7-(thiazol-2-yl)-[1,2,5]thiadiazolo[3,4-c]pyridine (M3), and 5-(thiazol-2-yl)-7H-

Table 1

Comparison of HOMO and LUMO energies calculated using various functionals with a fixed basis set (6-31G).

Functional	EXP	B3LYP	PBEPBE	WB97XD	B3PW91
HOMO	-5.43	-5.32	-4.7	-6.93	-5.34
LUMO	-3.35	-3.43	-3.86	-1.85	-3.54

silolo[3',4':5,6]naphtho[1,2-c][1,2,5]thiadiazole (M4). The modified structures of the designed molecules are depicted in Fig. 1. Additionally, optoelectronic parameters such as the frontier molecular orbitals (FMOs), HOMO-LUMO energy gap (E_g), density of states (DOS), UV-visible spectra, exciton binding energy (E_b), V_{OC} , electron-hole distribution heatmap, and electron density difference (EDD) were analyzed. Molecular dynamics (MD) simulations were performed to explore the intramolecular interactions and examine the structural stability of the system and its dynamic behavior [40]. These analyses aimed to illustrate the impact of the modifications on the electronic, photophysical, and photovoltaic properties of the designed molecules (M1–M4) in comparison with the reference molecule TPA-R. This study is a comprehensive extension of our previous research [41].

2. Computational formwork

2.1. Geometrical optimization

Throughout this study, all calculations were performed using the Gaussian 09 Revision D.02 software package [42], and the obtained results were visualized using Gauss View 6.0 [43]. Initially, geometric optimization of the reference TPA-R molecule was conducted using four different functionals, B3LYP [44], PBEPBE [45], WB97XD [46], and B3PW91 [47], at the DFT level with the 6-31G basis set (Table 1). Subsequently, the 3D structure was optimized using various basis sets such as 6-31G, 6-31G(d,p), 6-31+G(d,p), 6-311G, and def2-SVP (Table 2).

The reliability of the subsequent computational results depends on accurate optimization of the molecular geometries. Consequently, it is imperative to ascertain successful convergence of the geometry optimization procedure before proceeding with further calculations. This was achieved through frequency calculations, where the absence of imaginary frequencies unequivocally confirmed the attainment of a true energy minimum on the potential energy surface, thus validating the effectiveness of the geometry optimization process. The errors in

Table 2

Influence of basis set on HOMO and LUMO energies with B3LYP functional.

Basis set	EXP	6-31G	6-31G(d,p)	6-31+G(d,p)	6-311G	def2-SVP
HOMO	-5.43	-5.32	-5.27	-5.53	-5.43	-5.48
LUMO	-3.35	-3.43	-3.23	-3.52	-3.61	-3.41

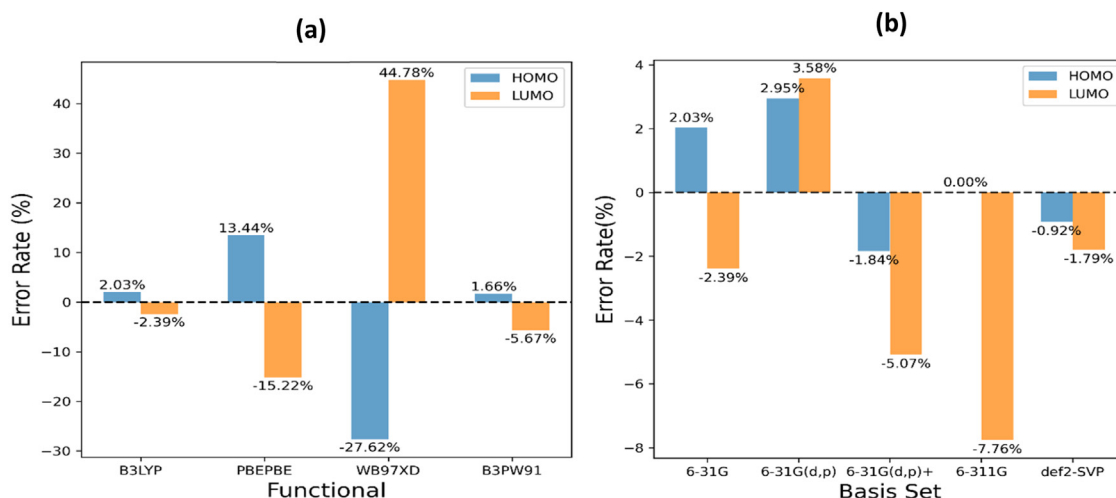


Fig. 2. Comparison of the percentage error in calculated HOMO and LUMO energies with experimental data: (a) for different functionals, and (b) using various basis sets.

the calculated HOMO values for TPA-R using the four aforementioned functionals with the same basis set were 2.03%, 13.44%, -27.62%, and 1.66%, respectively, compared to the experimental values. For the LUMO values, the errors were -2.39%, -15.22%, 44.78%, and -5.67%, respectively (as shown in Fig. 2(a)). These results indicate that B3LYP is the most accurate functional. In an identical procedure, the estimated errors between the experimental values of HOMO (-5.43 eV) and LUMO (-3.35 eV) for each basis set under the same functional (B3LYP) demonstrated that the def2-SVP basis set exhibits the lowest errors for HOMO and LUMO, with values of -0.92% and -1.49%, respectively, as illustrated in Fig. 2(b). The calculated HOMO and LUMO energies for the reference molecule, TPA-R, at the B3LYP/def2-SVP level of theory were in close agreement with the experimental values of the reference molecule. Following the validation of the theoretical method, we employed the B3LYP/def2-SVP level of theory to conduct further investigations on the novel designed molecules, M_i ($i = 1-4$).

2.2. Excited states

The optical properties and excited states of the studied molecules were obtained by TD-DFT calculations using the CAMB3LYP functional, which incorporates a long-range correction to accurately describe the excited states and transition energies [48]. Notably, in our previous work [49], the CAM-B3LYP/6-31G(d,p) level of theory showed strong agreement with the experimental results. This is further improved in this study, with the attainment of a maximum absorption wavelength (λ_{\max}) value of 572.28 nm, which closely aligns with the experimental value of 575 nm, representing a very small percentage error (0.47%). Additionally, the solvation mode within the TD-DFT framework was implicitly considered by employing a polarizable continuum model (PCM) with dichloromethane selected as the solvent. This choice was made to ensure the comparability between our theoretical and experimental results for the reference TPA-R.

2.3. Molecular dynamics simulations

MD simulations were conducted using Materials Studio (version 8.0) [50] to investigate the equilibrium configuration of the small molecule donors interacting with acceptor C70. Initially, a simulation box was constructed using 80 molecules of C70 and 50 small molecules to achieve a ratio of 1:1.6, which is consistent with the experimental scenario. This construction was carried out using the Amorphous Cell module, ensuring a density of 1 g/cm³. Subsequently, force-field-assigned charges and the COMPASS force field [51,52] were applied during the

dynamic simulation step by employing the NVT (constant particles number, volume, and temperature) ensemble to maintain optimum energy conditions, constant temperature, and volume. Both van der Waals and electrostatic interactions were accounted for using group-based summation methods.

3. Results and discussion

3.1. Frontier molecular orbitals analysis

FMO analysis reveals the energy gap ($E_g = E_{\text{LUMO}} - E_{\text{HOMO}}$) between HOMO and LUMO. The energy gap signifies the facility at which an electron can transition from HOMO to LUMO upon light absorption. This phenomenon occurs when the energy absorbed by the donor material from the solar spectrum matches or exceeds its bandgap energy. A smaller E_g translates into a lower energy for this electronic jump, which improves light absorption and, potentially, photovoltaic performance. The HOMO levels offer insight into the tendency of the molecule to donate electrons, demonstrating the electron-donating ability of the nucleophiles. Conversely, the LUMO levels indicate the capacity to accept electrons, demonstrating how electrophiles acquire electrons from nucleophiles. This information is crucial for understanding the charge transport within molecules, optical characteristics, electronic transitions, and chemical stabilities of organic molecules [53]. By optimizing the FMOs of organic molecules, materials that efficiently capture light, readily transition electrons to higher-energy states, and efficiently transport charges to generate electricity can be designed. Consequently, the HOMO and LUMO energy values, along with E_g , were computed for both the reference donor and hypothetical molecules to evaluate their suitability for organic photovoltaic applications. The results are summarized in Table 3.

Table 3

Energy of HOMOs, LUMOs, and E_g as calculated for the studied molecules at B3LYP/def2-SVP level of theory.

Molecules	E_{HOMO} (eV)	E_{LUMO} (eV)	E_g (eV)
TPA-R	-5.48 (-5.43) ¹	-3.41 (-3.35) ²	2.13
M1	-5.42	-3.86	1.56
M2	-5.32	-3.77	1.55
M3	-5.28	-3.71	1.57
M4	-5.26	-3.61	1.65

¹ Experimental energy value of the HOMO for TPA-R material.

² Experimental energy value of the LUMO for TPA-R material.

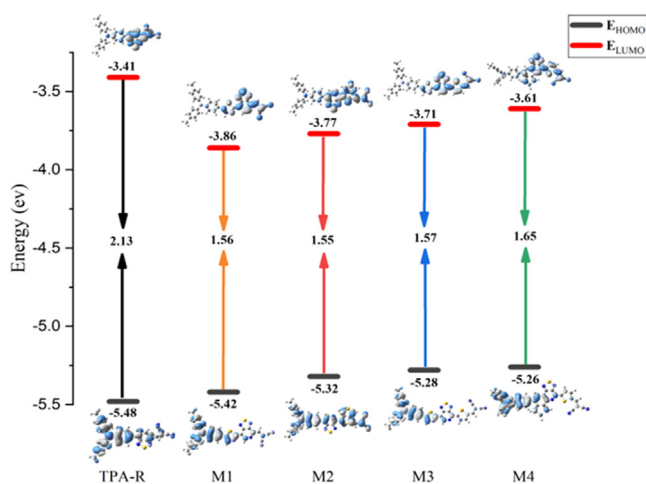


Fig. 3. Frontier molecular orbital energy diagrams and HOMO/LUMO isosurface representations of the SEDMs calculated at the B3LYP/def2-SVP level.

Our comprehensive analysis revealed that detailed electronic properties of SEDM are essential for their potential application in OSCs. Molecules M_i ($i = 1-4$) display E_{HOMO} values ranging from -5.42 to -5.26 eV and E_{LUMO} values ranging from -3.86 to -3.61 eV. The corresponding E_g values for these molecules range from 1.56 to 1.65 eV. In comparison, the reference molecule TPA-R exhibits E_{HOMO} and E_{LUMO} values of -5.48 and -3.41 eV, respectively, with an E_g of 2.13 eV. Analysis of these values indicates that molecule M1 has the lowest E_{HOMO} value (-5.42 eV), suggesting greater stability compared to the other molecules. Furthermore, the calculated E_g values for M2 (1.55 eV), M1 (1.56 eV), and M3 (1.57 eV) were remarkably similar, with differences well within the expected computational uncertainty associated with DFT-based methods. A smaller E_g signifies a lower energy requirement for electron excitation, which facilitates electron transfer processes within the material. Consequently, all molecules M1, M2, M3, and M4 molecules hold significant promise for efficient charge transport compared with the reference TPA-R. Additionally, in Fig. 3, it is evident that the HOMO distribution surface is predominantly localized on the donor moiety (triphenylamine) across all molecules, with a minor contribution from the first acceptor in M1 and M2. Conversely, the LUMO distribution surface was localized on the two acceptor parts of the molecules.

Analysis of the HOMO and LUMO levels was extended to SEDM:C70 systems to gain deeper insight into the separation of electron-hole pairs at the d-A interface. C70 was selected as the acceptor material to maintain consistency with the experimental conditions. The results depicted in Fig. 4 reveal a clear separation of the HOMO and LUMO wavefunctions, where the HOMOs are localized on the triphenyl-based small molecule donors, whereas the LUMOs are predominantly concentrated on the C70 acceptors, illustrating the effectiveness of intermolecular charge transfer across the d-A interface.

3.2. Density of state analysis

This section provides information on the orbitals, their importance to chemical bonding, and a detailed analysis of the electronic structure of M_i ($i = 1-4$) and TP-R using DOS plots (Fig. 5). A high DOS indicates the presence of several states at a particular energy level. Additionally, the positive DOS values were confirmed through a bonding interaction, whereas an anti-bonding interaction suggested that negative values and non-bonding interactions resulted in values near zero. In essence, the DOS provides insight into the total available space for the electronic states [54].

Our investigation focused on donor units in line with the d-A-A configuration, which significantly contributed to the frontier molecular or-

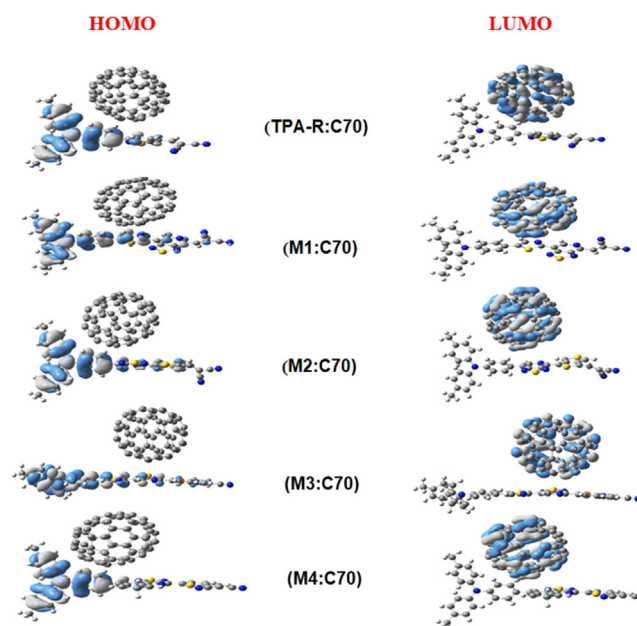


Fig. 4. 3D representation of the HOMO and LUMO of the SEDM:C70 complex, illustrating the spatial distribution and charge transfer direction at the d-A interface.

bitals across all studied molecules. Green represents the HOMO and red represents the LUMO. The density of localized states has a dramatically rising tendency to arise in the -7 to -15 eV range. The plots depict the orbital properties in the various energy ranges.

The heteroatoms present in the small molecules (S in M1 and M2, Se in M3, and additional N in M4) are expected to significantly influence the LUMO, stabilizing the negative charge and contributing to better electron mobility. Sulfur and selenium, which are softer atoms, promote charge delocalization and enhance the orbital overlap, which is crucial for charge transfer efficiency [55]. In M1 and M2, the sulfur atoms are expected to play a dominant role in the LUMO, facilitating electron transfer. M3, with selenium instead of sulfur, may exhibit a broader and more delocalized contribution to the LUMO, because selenium has a larger atomic radius and lower electronegativity. M4, which features an additional nitrogen atom in the acceptor group, can further stabilize the LUMO, leading to a narrower bandgap and improved electronic properties. Additionally, this finding is supported by the HOMO and LUMO energies, confirming the proximity of the frontier molecular orbitals in M1, M2, M3, and M4. Notably, modification of the reference molecule TPA-R enhanced the properties of the semiconductor M_i ($i = 1-4$), as evidenced by the reduced E_g .

3.3. Molecular electrostatic potentials

Molecular electrostatic potentials (MEPs) are useful tools for visualizing and understanding the distribution of electrostatic potentials around molecules. MEPs provide insight into the regions of a molecule that are favorable for electrophilic or nucleophilic attack, hydrogen bonding interactions, and reactivity [56]. The MEP maps (Fig. 6) are often colored according to a color scale, where the red regions represent areas with a high concentration of electrons, indicating potential sites for nucleophilic reactions. Nucleophiles, which are electron-rich species, are naturally drawn to these regions, where they can form new chemical bonds. In contrast, the blue regions indicate areas with lower electron densities, suggesting potential sites for electrophilic reactions. Electrophiles, which are electron-deficient species, are attracted to these regions, where they can bond with electron-rich species. The white regions represent areas of low or neutral potential. The interpretation of

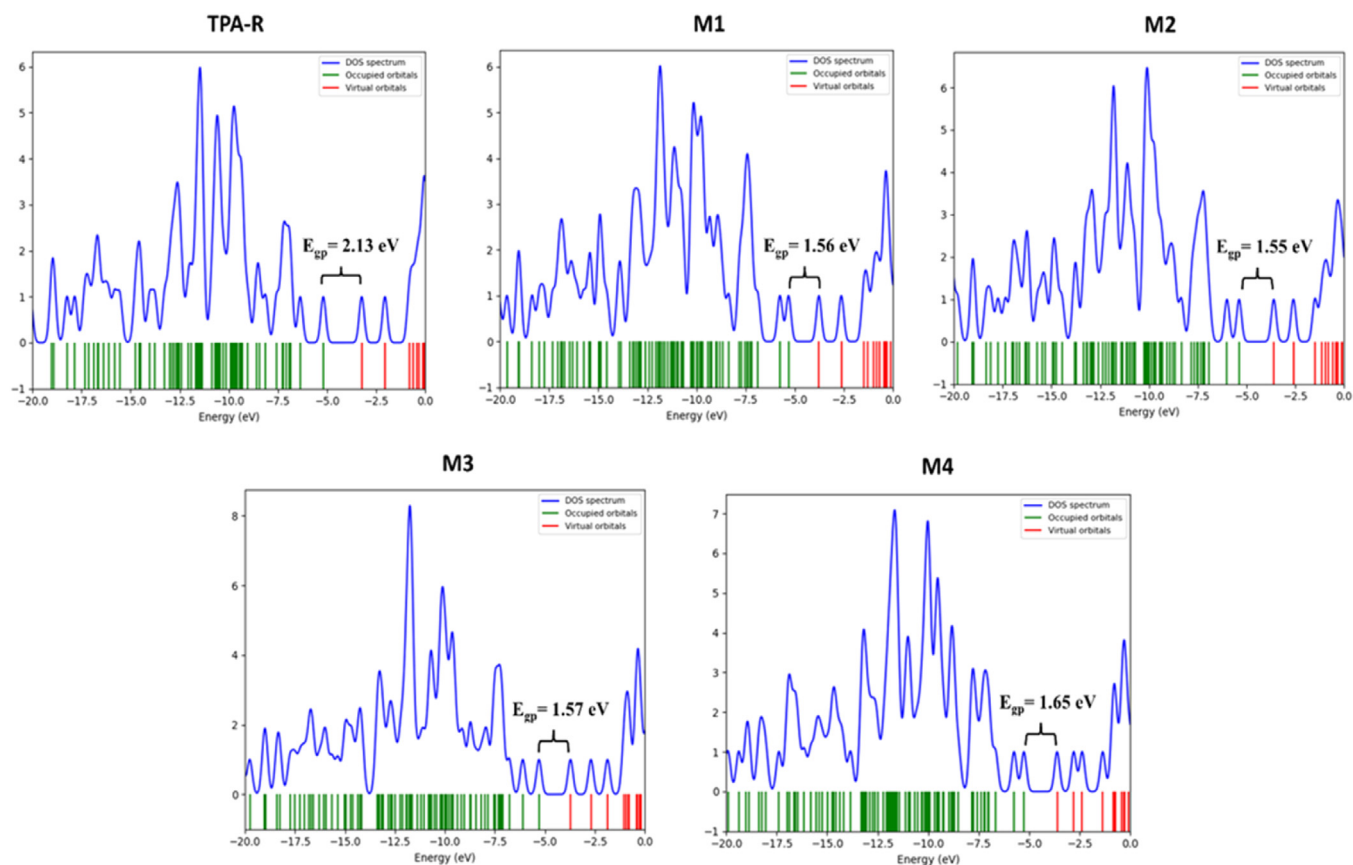


Fig. 5. DOS plots of the four designed molecules M_i ($i = 1-4$) and the reference molecule TPA-R.

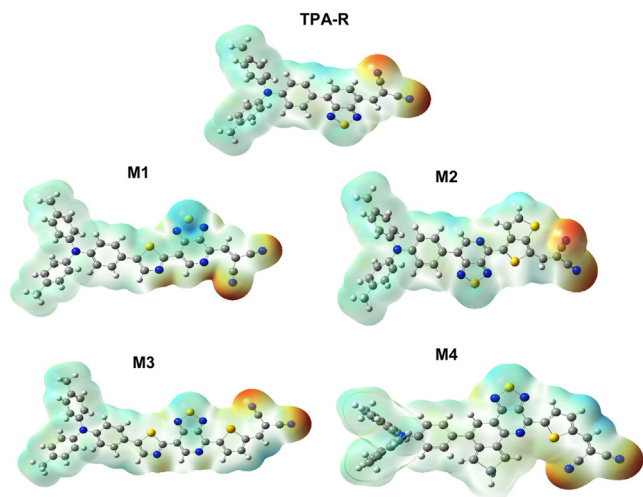


Fig. 6. 3D MEP maps of the designed materials M_i ($i = 1-4$) and TPA-R.

MEP maps enables the identification of probable sites for nucleophilic and electrophilic reactions within molecules, thereby assisting in the prediction of their reactivity across diverse chemical environments.

3.4. Optical properties

The optical properties of organic materials play a pivotal role in determining the efficiencies and functionalities of OSCs. First, these materials must effectively absorb sunlight across the visible and near-infrared spectra to initiate energy conversion. Second, upon the absorp-

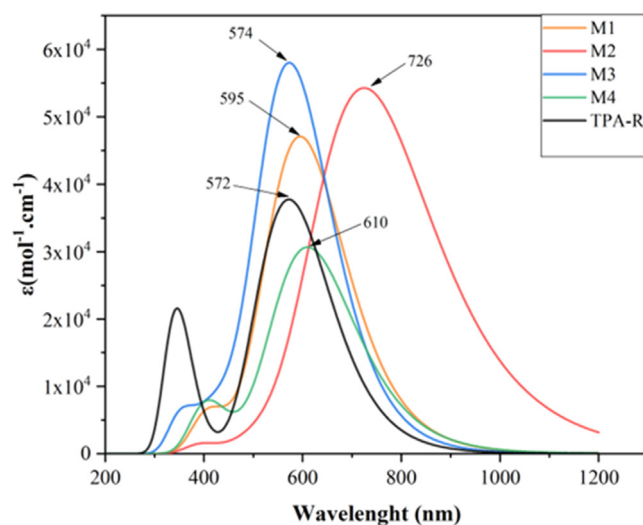


Fig. 7. Simulated absorption spectra of M1–M4 TPA-R at CAM-B3LYP/6–31G(d,p) level.

tion of photons, organic materials generate excitons, which are bound to electron-hole pairs. These properties were estimated at the theoretical level of TD-CAM-B3LYP/6–31G(d,p), and the corresponding results are summarized in Table 4.

The results obtained at the TD-CAM-B3LYP/6–31G(d,p) level of theory closely matched the experimental UV–vis spectrum of the reference molecule TPA-R. The theoretical analysis revealed that the maximum absorption λ_{\max} of TPA-R in dichloromethane using CPCM mode of sol-

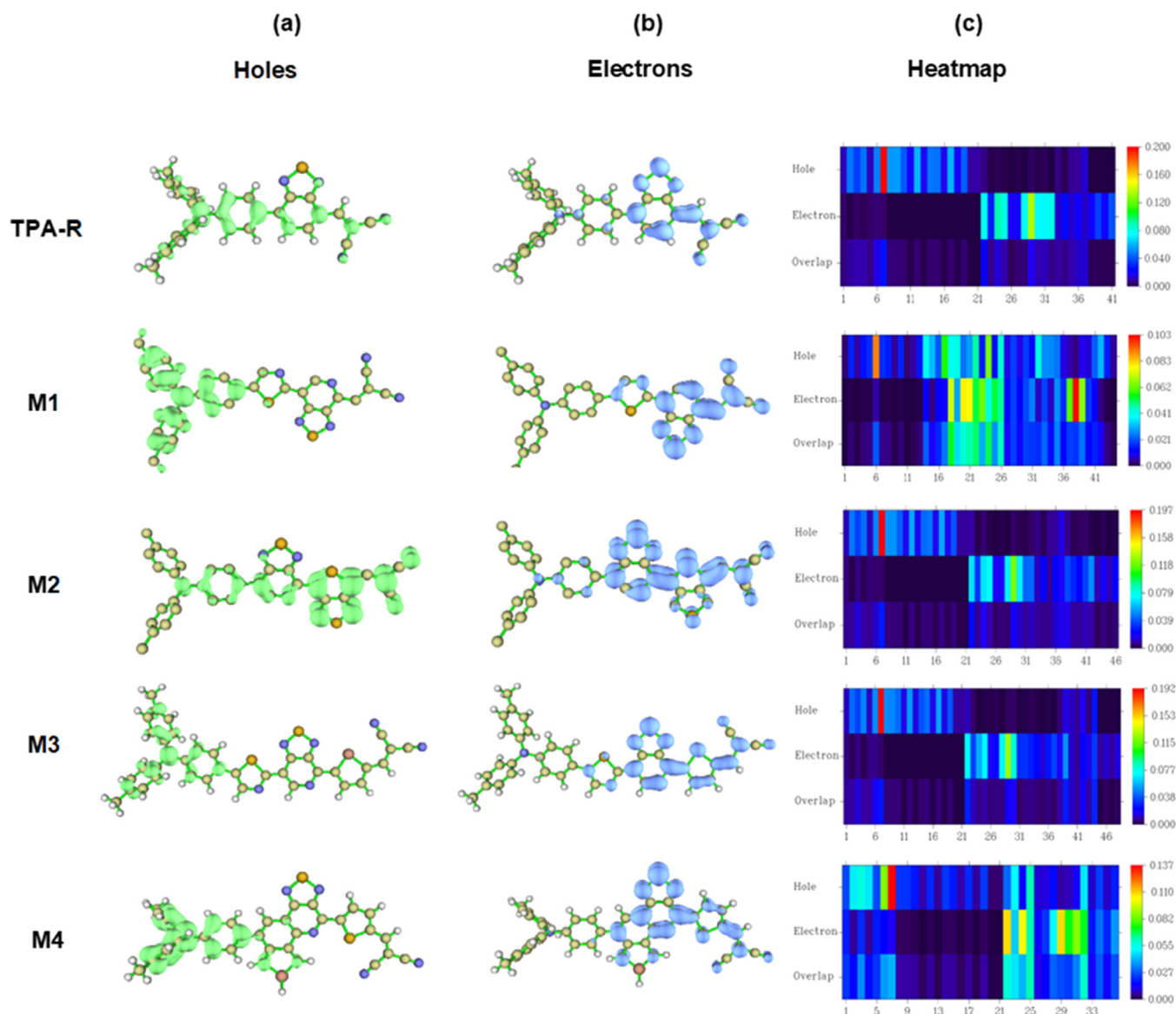


Fig. 8. Electron-holes distribution in the first excited state ($S_0 \rightarrow S_1$) of the SEDMs: (a) spatial localization of holes, (b) spatial localization of electrons, and (c) heat map showing electron-hole overlap, excluding hydrogen atom contributions.

Table 4

Calculated wavelength (λ_{\max}), oscillator strength (f), excitation energies (E_{ex}), dipole moment (D), and the percentage of electron transition (ETP) for the designed molecules at TD-CAM-B3LYP/6-31G(d,p) level in dichloromethane solvent.

Molecules	λ_{\max} (nm)	f (a.u.)	E_{ex} (eV)	ETP	D (Debye)
TPA-R	572.28 (570) ¹	0.9320	2.1660	H \rightarrow L(87%)	13.008
M1	595.34	1.1616	2.0820	H \rightarrow L(80%)	14.836
M2	726.34	1.3327	1.7070	H \rightarrow L(82%)	18.358
M3	574.22	1.4242	2.1592	H \rightarrow L(63%)	11.827
M4	610.36	0.7563	2.0313	H \rightarrow L(61%)	11.336

¹ The experimental value of λ_{\max} measured in dichloromethane (10^{-5} M).

vation is 572.28 nm, which is highly consistent with its experimental value of 570 nm, with a minimal error value of 0.4% [54]. This close agreement validated the appropriateness of the theoretical methods employed. Consequently, we employed this method (CAM-B3LYP/6-31G(d,p)) to investigate the optical properties of M1–M4 simultane-

ously. In the high-energy region (300–450 nm), the designed molecules exhibit secondary absorption peaks attributed to locally excited (LE) transitions. These transitions are primarily confined to specific molecular fragments such as the donor moieties or π -bridges units and typically involve $\pi-\pi^*$ transitions. These transitions exhibit lower oscillator strengths and limited charge-transfer characteristics. Their presence has been widely reported in d- π -A systems and reflects the multichromophoric and electronically rich architecture of the molecules [57,58]. In contrast, the dominant absorption bands observed in the lower-energy region (570–726 nm) were ascribed to ICT transitions characterized by a spatial shift in electron density from the donor to acceptor fragments. The simulated λ_{\max} for M1–M4, calculated at the TD-CAM-B3LYP/6-31G(d,p) level using the CPCM solvation model, range from 595 to 726 nm (Fig. 7). Compared to TPA-R ($\lambda_{\max} = 572$ nm), all designed compounds exhibit red-shifted and more intense ICT bands, reflecting enhanced d-A interaction and extended π -conjugation. Notably, M2 exhibited the most significant bathochromic shift, which was consistent with its lower excitation energy. Overall, the spectra of M1–M4 appear sharper and more intense than those of TPA-R, suggesting improved

charge-transfer efficiency and better light-harvesting potential. The oscillator strengths of the designed materials exhibit a notable increase, reaching a maximum value of 1.42 for M3. The f values for M1, M2, and M3 were 1.16, 1.33, and 1.42, respectively, all of which were higher than that of TPA-R ($f = 0.93$), indicating an enhanced light absorption capability. The electron transition percentage (ETP) associated with the HOMO→LUMO excitation ranges from 61% to 82% for the designed molecules. A higher ETP reflects a more dominant and well-defined orbital transition, which is generally correlated with efficient photoexcitation [59]. Although all designed molecules (M1–M4) exhibit slightly lower ETP values than TPA-R (87%), their high oscillator strengths indicated that the excitations remained efficient, highlighting the effectiveness of the molecular design.

3.5. Dipole moments

The dipole moments of TPA-R and its modified versions M_i revealed how structural modifications influence the overall polarity and charge distribution of the molecules, which are key factors in their electronic performance [60,61]. TPA-R, consists of a triphenylamine donor, a phenyl-first acceptor, and a benzothiadiazole-dicyanovinylene second acceptor, creating a balanced d-A-A system that results in a moderate dipole moment (13.008 D). M1 (14.836 D) showed an increased dipole moment, likely due to the replacement of benzothiadiazole with a thiadiazole-pyridine unit in the acceptor, enhancing the electron-withdrawing capability without major changes to the molecular geometry. This leads to a stronger charge separation. M2 (18.358 D) exhibited the highest dipole moment among the series, reflecting the strongest intramolecular charge transfer. This is attributed to the introduction of an additional thiophene ring in the first acceptor and a tetrazine unit in the second acceptor, which significantly amplifies the electron-withdrawing effect and facilitates charge delocalization through extended π -conjugation. In contrast, M3 (11.827 D) and M4 (11.336 D) exhibited lower dipole moments than TPA-R. For M3, replacement of the dicyanovinylene group with a less electron-withdrawing moiety likely resulted in a more balanced charge distribution. Similarly, M4 is a fused-ring system in the acceptor unit that may distribute the electron density more uniformly across the molecule despite the presence of electron-withdrawing groups. The consistent use of a triphenylamine donor across all the molecules ensures a stable electron-rich region, whereas variations in the first and second acceptor units fine-tune the electronic properties of the molecules. The phenyl bridge in TPA-R and M1 maintained planarity; however, the introduction of a thiophene ring in M2–M4 causes slight twisting, which could impact conjugation and charge transfer.

3.6. Electron-hole analysis

The 3D isosurfaces depicting holes and electrons, along with the distribution heat map, were generated using the methodology introduced by Chen et al., with the Multiwfn wavefunction analyzer [62]. Figs. 8(a)(b) show the isosurfaces representing the special localization of holes and electrons, with holes depicted in green and electrons depicted in blue. The corresponding distribution heatmaps of the electron-hole pairs are presented in Fig. 8(c), where the x-axis of the heat map corresponds to the number of atoms associated with each atom in the Gaussian09 Z matrix. The color scale on the right indicates the degree of contribution. The holes were predominantly localized in the donor part of the molecules, whereas electrons were prominently observed in acceptors 1 and 2. The D index provides a comprehensive assessment of the distance between the centroid of the electron and hole within the molecular system. A higher D value indicates a longer distance over which the charges can be effectively transferred. In our analysis, molecules M1, M2, M3, and M4 demonstrate significantly higher D values of 11.168, 6.114, 11.405, and 9.073 Å, respectively, compared to the reference

Table 5

Electron-hole separation indexes (D , t , Δr) and E_b for the first singlet excited state (S_1) of the SEDMs.

Molecule	D (Å)	t (Å)	Δr (Å)	E_b (eV)
TPA-R	4.052	0.412	3.459	3.21
M1	11.168	8.303	8.096	1.40
M2	6.114	4.651	5.995	1.87
M3	11.405	7.566	7.963	1.42
M4	9.073	5.827	6.601	1.70

molecule TPA-R (4.052 Å) (Table 5). The t index [63] serves as an additional metric for assessing the electron-hole separation. A positive t value indicates a distinct separation between the two charge carriers. The results presented in Table 5 indicate that all M_i ($i = 1-4$) exhibit larger t values (8.303, 4.651, 7.566, and 5.827 Å, respectively) than the TPA-R molecule, indicating a clearer separation of charge carriers within these molecules. The Δr index [64], another metric of charge transfers molecular excitations, provides a quantitative measure of an electron excitation mode, with a higher value ($\Delta r > 2.0$ Å) indicating a greater likelihood of the excitation being associated with a delocalized state. States with Δr index below 2.0 Å are typically classified as locally excited states. Table 5 shows the Δr index for TPA-R, M1, M2, M3, and M4, with values of 5.782, 8.096, 5.995, 7.963, and 6.601 Å, respectively, which are in good agreement with previous indices (D , t). This indicates that all molecules have a Δr index higher than 2.0 Å, suggesting effective charge transfer between the donor and acceptor fragments.

3.7. Hole-electron coulomb attractive energy

The efficiency of OSCs and the rate of charge separation depend on E_b , which is the energy required to separate an electron from a hole in an excitonic system [65]. These energies are crucial as they determine how effectively excitons, which are bound electron-hole pairs, can be dissociated into free charges for electrical conduction (Eq. (1)). The electron-hole interaction energy can be calculated using a simple Coulomb equation:

$$E_b = - \iint \frac{\rho^{\text{hole}}(r_1)\rho^{\text{ele}}(r_2)}{|r_1 - r_2|} dr_1 dr_2 \quad (1)$$

where E_b denotes the Coulomb interaction energy within a physical system. In this equation, $\rho^{\text{hole}}(r_1)$ signifies the charge density attributed to a

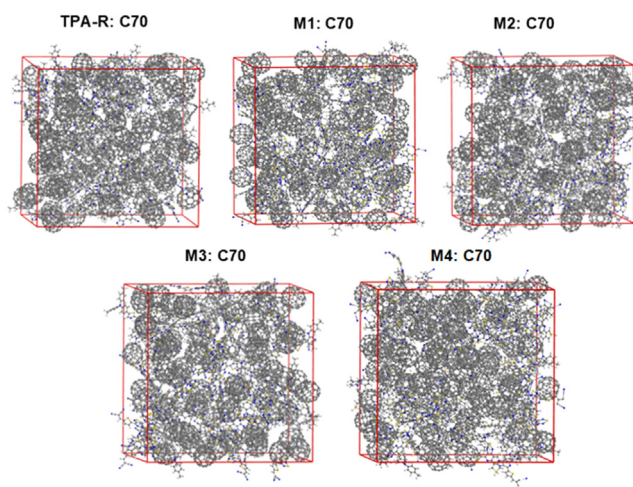


Fig. 9. Equilibrium configurations of the SEDM:C70 complexes obtained from MD simulations performed under the NVT ensemble using the COMPASS force field. The periodic boundary boxes are shown in red, illustrating the spatial distribution and packing behavior of the molecules.

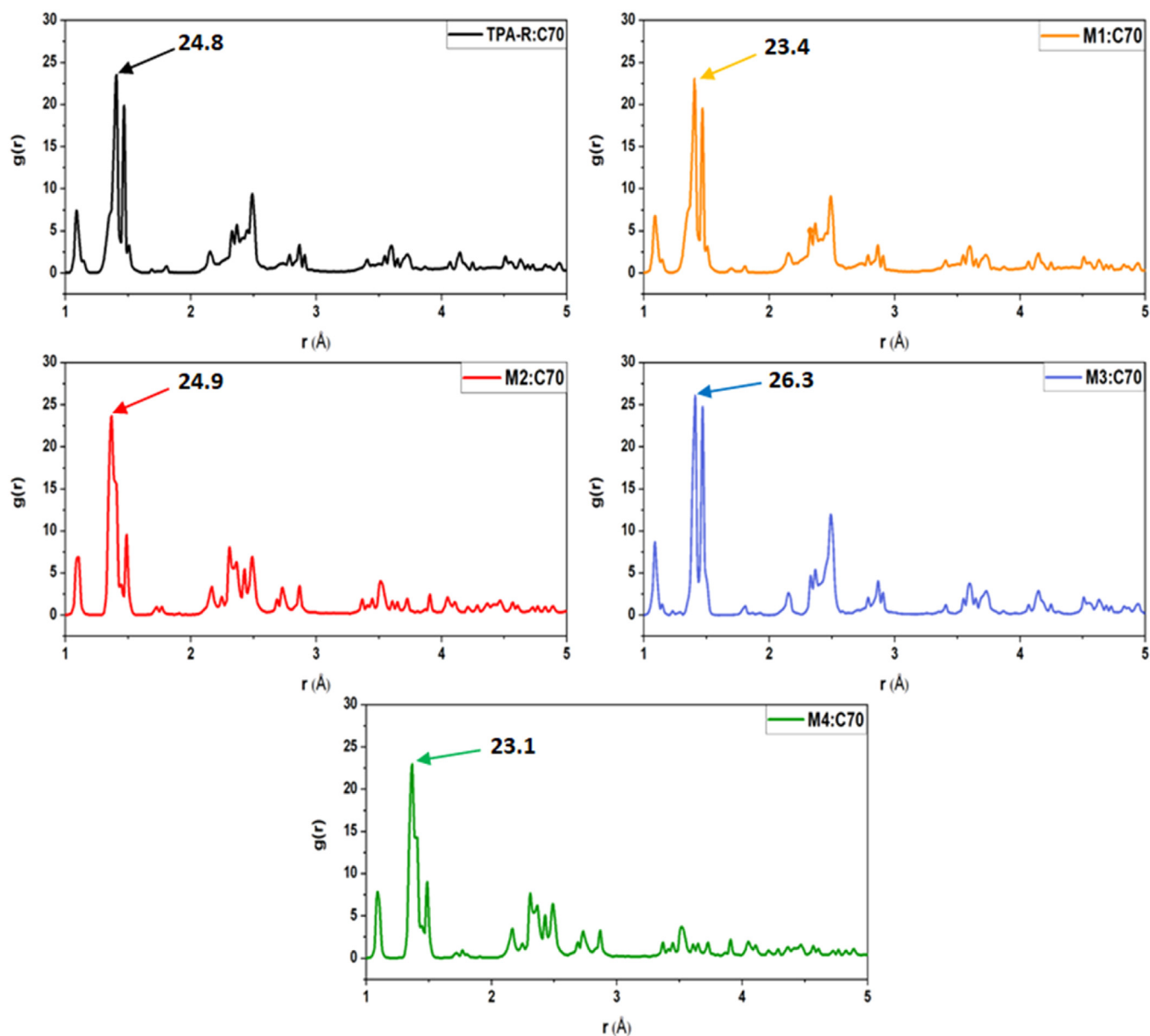


Fig. 10. RDF of the SEDM:C70 complex. The peaks in $g(r)$ indicate preferred intermolecular distances, reflecting the degree of structural ordering and interaction strength within each complex.

hole positioned at (r_1) . Conversely, $\rho^{\text{elec}}(r_2)$ represents the charge density corresponding to an electron located at (r_2) . The term $|r_1 - r_2|$ symbolizes the distance-separating positions r_1 and r_2 . The reduced electron-hole Coulomb attractive force leads to a decrease in the exciton binding energies. As shown in Table 5

Table 5, the reference molecule, TPA-R, exhibited an exciton binding energy of 3.21 eV, indicating a relatively strong electron-hole interaction within its structure. In comparison, all four molecules exhibited significantly lower exciton binding energies. Molecule M1 displayed a substantially lower exciton binding energy of 1.40 eV (a 56% decrease from TPA-R), suggesting a much weaker electron-hole interaction, which facilitates charge separation processes within the material. Similarly, M3 exhibits a comparable exciton binding energy of 1.42 eV (56% decrease), indicating an equally weak interaction. Molecule M4 displays an exciton binding energy of 1.70 eV (47% decrease), representing a moderate interaction strength, while M2 demonstrates an exciton binding energy of 1.87 eV (42% decrease). These reduced exciton bind-

ing energies across all the designed molecules suggest enhanced charge separation capabilities compared to those of TPA-R.

3.8. Molecular dynamics simulations

MD simulation is a computational technique used to study the behavior and interactions of molecules over time [66]. MD simulations provide a comprehensive understanding of molecular dynamics and rely heavily on the intricate interplay between various factors such as velocity, force fields, and types of molecular interactions. Velocity is a fundamental parameter representing the speed and direction of molecular motion in simulations. It plays a crucial role in determining the trajectory of molecules over time and influences their behavior and interactions. Force fields, on the other hand, are mathematical models used to describe the potential energy of a system as a function of atomic coordinates [67]. They encompass both bonded interactions, such as the stretching and bending of chemical bonds within molecules, and non-

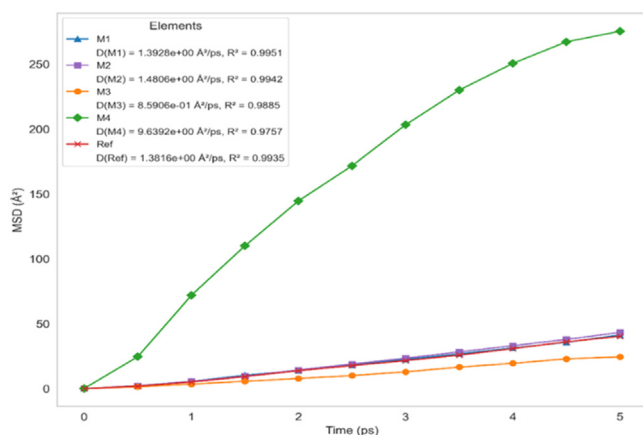


Fig. 11. MSD curves of the SEDMs in the presence of the fullerene acceptor C70.

bonded interactions, including electrostatic and van der Waals forces between atoms or molecules. The molecule-C70 system was meticulously constructed at a 1:1.6 ratio, ensuring that the molecular interactions and spatial arrangements in the simulation closely mirrored those observed in the experimental setup. The equilibrium configuration of the small donor molecules and their interaction with the acceptor C70 can be depicted through visualization within the simulation boxes (Fig. 9).

In MD simulations, the pair correlation function $g(r)$ or radial distribution function (RDF) is an important metric. It describes the average arrangement of atoms around a specific atom within a simulated system. It provides insights into how atoms are distributed in space relative to each other and indicates noncovalent interactions between molecules [68]. Mathematically, $g(r)$ is defined as the ratio of the probability density of finding particles at a distance r to the same probability density for a uniform particle distribution.

The RDF profiles of M1:C70 and M3:C70 showed similar general shapes and peak distributions, suggesting interaction characteristics comparable to those of TPA-R:C70. This resemblance can be attributed to the structural similarity of M1, M3, and TPA-R, particularly in their d-A frameworks. Similarly, M2:C70 and M4:C70 showed similar RDF profiles, reflecting parallel interaction behaviors, probably owing to their common molecular design features (Fig. 10). However, significant differences were observed in the intensity and shape of the first RDF peak, which corresponded to the strongest short-range interactions. M3 showed the highest and sharpest first peak, suggesting that it had the most localized and intense interaction with C70. TPA-R and M2 showed slightly reduced peak intensities, whereas M4 exhibited the lowest and broadest first peaks, indicating weaker localized interactions. These variations correlated with structural modifications in the acceptor groups of the molecules. Secondary peaks observed between 1.5–4 Å across all the systems indicate the presence of additional interaction shells. The consistent donor group likely contributes to similar overall RDF patterns, whereas differences in the acceptor groups appear to modulate the interaction strength. These findings suggest that while all molecules interact effectively with C70, the structural modifications in M1–M4 subtly alter the nature and strength of these interactions, potentially affecting their performance in optoelectronic applications.

3.9. Mean squared displacement and diffusion analysis

Mean square displacement (MSD) analysis provides a quantitative assessment of the diffusion behavior of d-A molecules M1–M4 in the presence of the C70 fullerene acceptor, offering an overview of the molecular mobility, intermolecular interactions, and their potential implications for charge transport in OSCs. As shown in Fig. 11, different

diffusion trends were observed for the studied molecules. The exceptional mobility of M4 is attributed to the steric effect induced by the SiH₂ group. This group disrupts the non-covalent interactions between the molecule and the C₇₀ fullerene by reducing the possibility of close π - π stacking. As a result, M4 exhibited faster diffusion, confirmed by the highest diffusion coefficient ($D = 9.6392 \text{ \AA}^2/\text{ps}$), which suggests a weaker interaction with the fullerene cage. While higher mobility can facilitate charge carrier transport, excessive diffusivity can perturb d-A interactions, potentially compromising the charge separation efficiency. Conversely, M3 had the lowest diffusion coefficient ($0.8590 \text{ \AA}^2/\text{ps}$), suggesting a stronger interaction with C70, which aligns with the finding in RDF results. This behavior may be associated with the Se-containing acceptor unit, which increases the molecular rigidity and limits diffusion. Although a stronger d-A interaction could improve charge separation, reduced molecular mobility could hinder charge carrier transport, which could limit the photovoltaic performance. M1 and M2 exhibited moderate diffusion coefficients of 1.3928 and 1.4806 $\text{\AA}^2/\text{ps}$, respectively, which are close to that of TPA-R (1.3816 $\text{\AA}^2/\text{ps}$). The structural modifications of these molecules did not significantly alter their interactions with C70. However, the presence of a cyano substituent (–CN) in M1 and M2 may have contributed to a slight increase in mobility, probably because of a minor reduction in the intermolecular bond strength. The reliability of the diffusion coefficients was confirmed by analyzing the coefficient of determination (R^2), which reflects the linearity of the MSD curves. All the molecules studied had R^2 values greater than 0.97, which guaranteed that the extracted diffusion coefficients accurately represent their mobility behaviors. These diffusion characteristics have direct implications for charge transport in OSCs, where an optimal balance between the molecular mobility and d-A interactions is essential. Although a high diffusion coefficient, such as that of M4, can enhance charge transport, excessive mobility can lead to inefficient charge separation. Conversely, a lower diffusion coefficient, as in the case of M3, can improve charge separation but limits charge carrier mobility. The intermediate diffusivities of M1 and M2 suggest that these molecules achieved a balanced compromise between charge separation and transport efficiency.

3.10. Comparative evaluation of key properties

To consolidate and clarify the selection of M1 and M2 as the most promising donor materials, a comparative heat map (Fig. 12) was constructed to summarize the normalized values of several key descriptors influencing the performance of OSCs. These include E_g , λ_{max} , f , E_{ex} , E_b , Δr , dipole moment, and the maximum value of the $g(r)$, which reflects the strength of d-A interactions. For the parameters in which lower values were favorable (E_g , E_{ex} , and E_b), the scale was inverted before normalization. For any given parameter x , the normalized value x_{norm} was calculated using the following formula:

$$x_{\text{norm}} = \frac{x - x_{\text{min}}}{x_{\text{max}} - x_{\text{min}}} \quad (2)$$

As shown in Fig. 12, M1 and M2 consistently achieved the highest normalized values across multiple parameters, indicating a well-balanced combination of desirable characteristics. M1 stands out with high f , low E_b , and excellent charge separation metrics (Δr and D), leading to a strong overall performance profile. M2, exhibited the best performance in light absorption (λ_{max}), dipole moment, and charge separation, with a slight trade-off in exciton binding energy. Both molecules maintained relatively high scores for interaction strength $g(r)$, suggesting efficient electron transfer with the C70 acceptor.

In contrast, M3 achieved high d-A interaction strength but lower normalized values in E_b and Δr , which may hinder its overall charge transport efficiency. M4 displayed moderate performance across most criteria; however, it lacked standout features in key areas, such as absorption intensity and exciton dissociation. The reference molecule TPA-R registered the lowest cumulative normalized scores, particularly in terms of

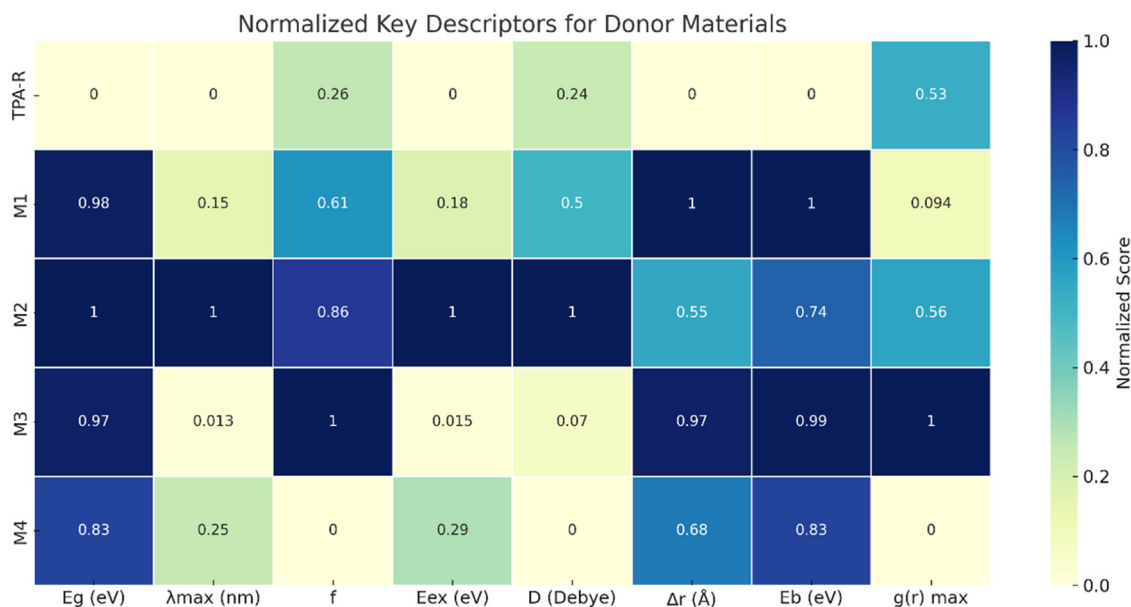


Fig. 12. Comparative heatmap of key properties for TPA-R and M1–M4. Dark blue indicates the most favorable performance (values close to 1), while light yellow represents the least favorable (values close to 0).

charge separation and exciton binding energy, reinforcing its role as a baseline rather than a high-performance candidate.

4. Conclusion

In this study, four small donor materials with promising properties were successfully designed by modifying the acceptor moiety of the reference molecule TPA-R through the incorporation of four different fragments containing sulfur heterocycles, selenophene, and thiadiazole. Analysis of the HOMO and LUMO levels demonstrated that our computational approach, employing the DFT method at the B3LYP/def2-SVP level of theory, was highly accurate and in good agreement with the experimental data, exhibiting a minimum error. Furthermore, these modifications led to a considerable reduction in E_g , demonstrating their effectiveness for applications in OSCs. DOS and MEP were used to analyze the electronic distribution and morphology of the designed materials. Furthermore, the UV-visible spectra predicted using the TD-CAM-B3LYP/6-31G(d,p) approach were found to be highly accurate with the experimental λ_{max} value, and the designed donor materials M1–M4 showed red-shifted absorption compared to the reference molecule TPA-R. Moreover, the electron-hole transfer mechanism from the donor to the acceptor unit was elucidated. The results of the polarity indices indicate that all molecules M1–M4 exhibit higher mobility of the electron-hole pair, facilitating their separation. The interaction between the donor molecule SEDM and the fullerene acceptor C70 was investigated using MD simulations and RDF-MSD analyses to assess the intermolecular interactions and molecular mobility. The results indicate that M1 and M2 exhibit a moderate balance between interaction strength and mobility, suggesting that these molecules maintain stable d-A interactions while allowing sufficient diffusion for effective charge transport. Notably, M1 and M2 were found to be suitable for applications in organic photovoltaics owing to their favorable optoelectronic properties and potential for efficient charge transfer processes.

Declaration of Competing Interest

The authors declare that they have no known competing financial interests or personal relationships that could have appeared to influence the work reported in this paper.

CRediT authorship contribution statement

Mohammed Elkabous: Writing – review & editing, Writing – original draft, Visualization, Validation, Software, Resources, Methodology, Investigation, Conceptualization. **Mohammed Ouachekradi:** Writing – review & editing, Writing – original draft, Visualization, Validation, Investigation, Conceptualization. **Yasser Karzazi:** Writing – review & editing, Writing – original draft, Visualization, Validation, Supervision, Investigation, Conceptualization.

Acknowledgements

We gratefully acknowledge the support of the Center for Doctoral Studies (CEDOC) at University Mohammed I. We also extend our sincere gratitude to the reviewers for their valuable comments and suggestions, which have significantly enhanced the clarity and scientific rigor of this study.

References

- [1] J.C. Bernede, Organic photovoltaic cells: History, principle and techniques, *J. Chil. Chem. Soc.* 53 (2008) 1549–1564, doi:10.4067/S0717-97072008000300001.
- [2] Y. Liang, P. Deng, Z. Wang, Z. Guo, Y. Lei, Novel perylene diimide acceptor for nonfullerene organic solar cells, *Funct. Mater. Lett.* 12 (2019) 1950022, doi:10.1142/S179360471950022X.
- [3] E.K. Solak, E. Irmak, Advances in organic photovoltaic cells: A comprehensive review of materials, technologies, and performance, *RSC Adv.* 13 (2023) 12244–12269, doi:10.1039/D3RA01454A.
- [4] S.R. Forrest, The limits to organic photovoltaic cell efficiency, *MRS. Bull.* 30 (2005) 28–32, doi:10.1557/MRS2005.5.
- [5] N. Chander, S. Singh, S.S.K. Iyer, Stability and reliability of P3HT:PC61BM inverted organic solar cells, *Sol. Energy. Mater. Sol. Cells.* 161 (2017) 407–415, doi:10.1016/j.solmat.2016.12.020.
- [6] S.K. Gupta, R.K. Gupta, K.S. Nalwa, A. Garg, Inverted PTB7-Th:PC71BM organic solar cells with 11.8% PCE via incorporation of gold nanoparticles in ZnO electron transport layer, *Sol. Energy.* 214 (2021) 220–230, doi:10.1016/j.solener.2020.11.071.
- [7] A.J. Clarke, J. Luke, R. Meitzner, J. Wu, Y. Wang, H.K.H. Lee, E.M. Speller, H. Britton, H. Cha, M.J. Newman, K. Hooper, A. Evans, F. Gao, H. Hoppe, I. McCulloch, U.S. Schubert, T.M. Watson, J.R. Durrant, W.C. Tsoi, J.S. Kim, Z. Li, Non-fullerene acceptor photostability and its impact on organic solar cell lifetime, *Cell. Rep. Phys. Sci.* 2 (2021) 100498, doi:10.1016/j.xcrp.2021.100498.
- [8] B.H. Jiang, C.P. Chen, H.T. Liang, R.J. Jeng, W.C. Chien, Y.Y. Yu, The role of Y6 as the third component in fullerene-free ternary organic photovoltaics, *Dyes. Pigm.* 181 (2020) 108613, doi:10.1016/j.dyepig.2020.108613.
- [9] T. Liu, T. Yang, R. Ma, L. Zhan, Z. Luo, G. Zhang, Y. Li, K. Gao, Y. Xiao, J. Yu, X. Zou, H. Sun, M. Zhang, T.A. Dela Peña, Z. Xing, H. Liu, X. Li, G. Li, J. Huang,

- C. Duan, K.S. Wong, X. Lu, X. Guo, F. Gao, H. Chen, F. Huang, Y. Li, Y. Li, Y. Cao, B. Tang, H. Yan, 16% efficiency all-polymer organic solar cells enabled by a finely tuned morphology via the design of ternary blend, *Joule* 5 (2021) 914–930, doi:10.1016/j.joule.2021.02.002.
- [10] T. Zhang, C. An, P. Bi, Q. Lv, J. Qin, L. Hong, Y. Cui, S. Zhang, J. Hou, A thiadiazole-based conjugated polymer with ultradeep HOMO level and strong electroluminescence enables 18.6% efficiency in organic solar cell, *Adv. Energy Mater.* 11 (2021) 2101705, doi:10.1002/aenm.202101705.
- [11] X. He, L. Yin, Y. Li, Design of organic small molecules for photovoltaic application with high open-circuit voltage (Voc), *J. Mater. Chem. C* 7 (2019) 2487–2521, doi:10.1039/c8tc06589f.
- [12] Q.L. Huang, H.X. Li, Recent progress of bulk heterojunction solar cells based on small-molecular donors, *Chin. Sci. Bull.* 58 (2013) 2677–2685, doi:10.1007/s11434-013-5930-z.
- [13] M.U. Khan, M. Khalid, M.N. Arshad, M.N. Khan, M. Usman, A. Ali, B. Saifullah, Designing star-shaped subphthalocyanine-based acceptor materials with promising photovoltaic parameters for non-fullerene solar cells, *ACS Omega* 5 (2020) 23039–23052, doi:10.1021/acsomega.0c02766.
- [14] J. Yang, B. Xiao, A. Tang, J. Li, X. Wang, E. Zhou, Aromatic-diimide-based n-type conjugated polymers for all-polymer solar cell applications, *Adv. Mater.* 31 (2019) 1804699, doi:10.1002/adma.201804699.
- [15] C. Liu, L. Shao, S. Chen, Z. Hu, H. Cai, F. Huan, Recent progress in π -conjugated polymers for organic photovoltaics: Solar cells and photodetectors, *Prog. Polym. Sci.* 143 (2023) 101711, doi:10.1016/j.progpolymsci.2023.101711.
- [16] S. Himmelberger, A. Salloeo, Engineering semiconducting polymers for efficient charge transport, *MRS Commun.* 5 (2015) 383–395, doi:10.1557/mrc.2015.44.
- [17] Y. Cui, H. Yao, B. Gao, Y. Qin, S. Zhang, B. Yang, C. He, B. Xu, J. Hou, Fine-tuned photoactive and interconnection layers for achieving over 13% efficiency in a fullerene-free tandem organic solar cell, *J. Am. Chem. Soc.* 139 (2017) 7302–7309, doi:10.1021/jacs.7b01493.
- [18] G. Zhang, K. Zhang, Q. Yin, X.F. Jiang, Z. Wang, J. Xin, W. Ma, H. Yan, F. Huang, Y. Cao, High-performance ternary organic solar cell enabled by a thick active layer containing a liquid crystalline small molecule donor, *J. Am. Chem. Soc.* 139 (2017) 2387–2395, doi:10.1021/jacs.6b11991.
- [19] D. Deng, Y. Zhang, J. Zhang, Z. Wang, L. Zhu, J. Fang, B. Xia, Z. Wang, K. Lu, W. Ma, Z. Wei, Fluorination-enabled optimal morphology leads to over 11% efficiency for inverted small-molecule organic solar cells, *Nat. Commun.* 7 (2016) 13740, doi:10.1038/ncomms13740.
- [20] D. Deb, K. Bhargava, Next generation photovoltaics, in: D. Deb, K. Bhargava (Eds.), *Degradation, Mitigation, and Forecasting Approaches in Thin Film Photovoltaics*, Academic Press, United Kingdom, 2022, pp. 151–160, doi:10.1016/B978-0-12-823483-9.00020-6.
- [21] N.K. Elumalai, A. Uddin, Open circuit voltage of organic solar cells: An in-depth review, *Energy. Env. Sci.* 9 (2016) 391–410, doi:10.1039/C5EE02871J.
- [22] L. Liu, Y. Kan, K. Gao, J. Wang, M. Zhao, H. Chen, C. Zhao, T. Jiu, A.K.Y. Jen, Y. Li, Graphdiyne derivative as multifunctional solid additive in binary organic solar cells with 17.3% efficiency and high reproductivity, *Adv. Mater.* 32 (2020) 1907604, doi:10.1002/adma.201907604.
- [23] M.U. Khan, M.Y. Mehboob, R. Hussain, R. Fatima, M.S. Tahir, M. Khalid, A.A.C. Brag, Molecular designing of high-performance 3D star-shaped electron acceptors containing a truxene core for nonfullerene organic solar cells, *J. Phys. Org. Chem.* 34 (2021) e4119, doi:10.1002/poc.4119.
- [24] X.K. Chen, V. Coropceanu, J.L. Brédas, Assessing the nature of the charge-transfer electronic states in organic solar cells, *Nat. Commun.* 9 (2018) 5295, doi:10.1038/s41467-018-07707-8.
- [25] F. Bureš, Fundamental aspects of property tuning in push-pull molecules, *RSC Adv.* 4 (2014) 58826–58851, doi:10.1039/C4RA11264D.
- [26] M. Ouachekradi, M. Elkabous, Y. Karzazi, Molecular engineering of phenothiazine-based D-A- π -A sensitizers: A quantum chemical study on the role of auxiliary acceptors in improving DSSC efficiency, *J. Ind. Eng. Chem.* (2025), doi:10.1016/j.jiec.2025.04.052.
- [27] J. Wang, V. Gadenne, L. Patrone, J.M. Raimundo, Self-assembled monolayers of push-pull chromophores as active layers and their applications, *Molecules* 29 (2024) 559, doi:10.3390/molecules29030559.
- [28] M. Elkabous, Y. Karzazi, Exploring the applicability of novel indolic semiconductors in dye-sensitized solar cells: Theoretical forecasting and assessment of electron injection into TiO₂, in: *Springer Proceedings in Energy*, 2024, pp. 369–376, doi:10.1007/978-3-031-57022-3_45.
- [29] M. Ouachekradi, M. Elkabous, Y. Karzazi, Theoretical study on the efficiency of new organic dyes based on (E)-2-(2-(thiophen-3-yl)vinyl)-1,1'-bipyrrrole as dye-sensitized solar cell sensitizers, *Chem. Phys. Mater.* 3 (2024) 440–450, doi:10.1016/j.chphma.2024.06.008.
- [30] H.C. Ting, Y.H. Chen, L.Y. Lin, S.H. Chou, Y.H. Liu, H.W. Lin, K.T. Wong, Benzochalcogenodiazole-based donor-acceptor-acceptor molecular donors for organic solar cells, *ChemSusChem* 7 (2014) 457–465, doi:10.1002/cssc.201301090.
- [31] P. Shen, H. Wang, P. Liao, L. Wang, Electronic properties of donor:acceptor complexes in all-polymer solar cells based on density functional theory, *J. Phys. D: Appl. Phys.* 54 (2021) 195301, doi:10.1088/1361-6463/abdffc.
- [32] M. Bourass, A.T. Benjelloun, M. Benzakour, M. Mcharfi, M. Hamidi, S.M. Bouziane, M. Bouachrine, DFT and TD-DFT calculation of new thienopyrazine-based small molecules for organic solar cells, *Chem. Cent. J.* 10 (2016) 67, doi:10.1186/s13065-016-0216-6.
- [33] A. Mahmood, M.I. Abdullah, S.U.D. Khan, Enhancement of nonlinear optical (NLO) properties of indigo through modification of auxiliary donor, donor and acceptor, *Spectrochim. Acta. Mol. Biomol. Spectrosc.* 139 (2015) 425–430, doi:10.1016/j.saa.2014.12.038.
- [34] M. Raftani, T. Abram, A. Azaïd, R. Kacimi, M.N. Bennani, M. Bouachrine, Theoretical design of new organic compounds based on diketopyrrolopyrrole and phenyl for organic bulk heterojunction solar cell applications: DFT and TD-DFT study, *Mater. Today. Proc.* 45 (2021) 7334–7343, doi:10.1016/j.matpr.2020.12.1228.
- [35] S.A.H. Vuai, M.S. Khalfan, N.S. Babu, DFT and TD-DFT studies for optoelectronic properties of coumarin-based donor- π -acceptor (D- π -A) dyes: Applications in dye-sensitized solar cells (DSSCs), *Heliyon* 7 (2021) e08339, doi:10.1016/j.heliyon.2021.e08339.
- [36] Y. Ren, M.Y. Li, Y.X. Song, M.Y. Sui, G.Y. Sun, X.C. Qu, P. Xie, J.L. Lu, Refined standards for simulating UV-vis absorption spectra of acceptors in organic solar cells by TD-DFT, *J. Photochem. Photobiol. Chem.* 407 (2021) 113087, doi:10.1016/j.jphotochem.2020.113087.
- [37] D. Khlaifia, M. Chemek, K. Alimi, DFT/TDDFT approach: An incredible success story in prediction of organic materials properties for photovoltaic application, *Moroc. J. Chem.* 8 (2020) 683–699, doi:10.48317/IMIST.PRSM/morjchem-v8i3.18518.
- [38] M. Ouachekradi, M. Elkabous, Y. Karzazi, Triphenylamine-based D-A- π -A dyes for DSSC applications: Theoretical study on the impact of auxiliary acceptor groups and π -bridges on photovoltaic performance using DFT and TD-DFT calculations, *J. Photochem. Photobiol. Chem.* 461 (2025) 116152, doi:10.1016/j.jphotochem.2024.116152.
- [39] Y.H. Chen, L.Y. Lin, C.W. Lu, F. Lin, Z.Y. Huang, H.W. Lin, P.H. Wang, Y.H. Liu, K.T. Wong, J. Wen, D.J. Miller, S.B. Darling, Vacuum-deposited small-molecule organic solar cells with high power conversion efficiencies by judicious molecular design and device optimization, *J. Am. Chem. Soc.* 134 (2012) 13616–13623, doi:10.1021/ja301872s.
- [40] I. El Bojaddayni, Y. El Ouadi, M. Elkabous, N. Achalhi, A. Yousuf, Y. Karzazi, A. Ouammou, S. Virolainen, Dynamic simulation-driven analysis of cadmium, nickel, cobalt, and iron adsorption mechanisms in zeolite LTA synthesized from bentonite, *Microporous. Mesoporous. Mater.* 384 (2025) 113433, doi:10.1016/j.micromeso.2024.113433.
- [41] M. Elkabous, A. Karzazi, Y. Karzazi, Deep learning-driven QSPR models for accurate properties estimation in organic solar cells using extended connectivity fingerprints, *Comput. Mater. Sci.* 243 (2024) 113146, doi:10.1016/j.commatsci.2024.113146.
- [42] M.J. Frisch, G.W. Trucks, H.B. Schlegel, G.E. Scuseria, M.A. Robb, J.R. Cheeseman, G. Scalmani, V. Barone, B. Mennucci, G.A. Petersson, H. Nakatsuji, M. Caricato, X. Li, H.P. Hratchian, A.F. Izmaylov, J. Bloino, G. Zheng, J.L. Sonnenberg, M. Hada, M. Ehara, K. Toyota, R. Fukuda, J. Hasegawa, M. Ishida, T. Nakajima, Y. Honda, O. Kitao, H. Nakai, T. Vreven, J.A. Montgomery Jr., J.E. Peralta, F. Ogliaro, M. Bearpark, J.J. Heyd, E. Brothers, K.N. Kudin, V.N. Staroverov, R. Kobayashi, J. Normand, K. Raghavachari, A. Rendell, J.C. Burant, S.S. Iyengar, J. Tomasi, M. Cossi, N. Rega, J.M. Millam, M. Klene, J.E. Knox, J.B. Cross, V. Bakken, C. Adamo, J. Jaramillo, R. Gomperts, R.E. Stratmann, O. Yazyev, A.J. Austin, R. Cammi, C. Pomelli, J.W. Ochterski, R.L. Martin, K. Morokuma, V.G. Zakrzewski, G.A. Voth, P. Salvador, J.J. Dannenberg, S. Dapprich, A.D. Daniels, O. Farkas, J.B. Foresman, J.V. Ortiz, J. Cioslowski, D.J. Fox, gaussian 09, Gaussian, Inc., Wallingford CT, 121 (2009) 150–166.
- [43] R. Dennington, T.A. Keith, J.M. Millam, *GaussView. Version 6* (2019).
- [44] M. El Ghozliani, M. Ouachekradi, R. Elkacmi, Y. Karzazi, A. Zeroual, K.J. Bonsy, E.G. Jayasree, E.M. Rakib, Indium-catalyzed reductive synthesis of 4-pyrrolyl-N-methyl-indazoles: DFT, molecular docking, and ADME-tox studies for antibacterial and anticancer drug discovery, *J. Mol. Struct.* 1340 (2025) 142486, doi:10.1016/j.molstruc.2025.142486.
- [45] M.Doust Mohammadi, H.Y. Abdullah, The adsorption of bromochlorodifluoromethane on pristine, Al, Ga, P, and As-doped boron nitride nanotubes: A study involving PBC-DFT, NBO analysis, and QTAIM, *Comput. Theor. Chem.* 1193 (2021) 113047, doi:10.1016/j.comptc.2020.113047.
- [46] J.D. Chai, M. Head-Gordon, Long-range corrected hybrid density functionals with damped atom-atom dispersion corrections, *Phys. Chem. Chem. Phys.* 10 (2008) 6615–6620, doi:10.1039/b810189b.
- [47] A.D. Becke, Density-functional thermochemistry. III. The role of exact exchange, *J. Chem. Phys.* 98 (1993) 5648–5652, doi:10.1063/1.464913.
- [48] T. Yanai, D.P. Tew, N.C. Handy, A new hybrid exchange–correlation functional using the coulomb-attenuating method (CAM-B3LYP), *Chem. Phys. Lett.* 393 (2004) 51–57, doi:10.1016/j.cplett.2004.06.011.
- [49] M. Elkabous, Y. Karzazi, Theoretical study of new 3-(methylthio)-8-phenyl-8H-thieno[2,3-b]indole derivatives for application in DSSC: Solvent effect, adsorption process on the surface of TiO₂, *Arab. J. Chem.* 17 (2024) 105457, doi:10.1016/j.arabjc.2023.105457.
- [50] Materials Studio package, BIOVIA, Dassault Systèmes, San Diego, USA (2017).
- [51] H. Sun, COMPASS: An ab initio force-field optimized for condensed-phase applications. Overview with details on alkane and benzene compounds, *J. Phys. Chem. B* 102 (1998) 7338–7364, doi:10.1021/jp980939v.
- [52] S.W. Bunte, H. Sun, Molecular modeling of energetic materials: The parameterization and validation of nitrate esters in the COMPASS force field, *J. Phys. Chem. B* 104 (2000) 2477–2489, doi:10.1021/jp991786u.
- [53] Z. El Aslaoui, Y. Karzazi, Molecular design of new π -conjugated materials based on pyrimidine for organic solar cells application, *Moroc. J. Chem.* 4 (2016) 838–848, doi:10.48317/IMIST.PRSM/morjchem-v4i3.5998.
- [54] N.S. Babu, Donor-acceptor-donor (D-A-D) structural monomers as donor materials in polymer solar cells: A DFT/TDDFT approach, *Des. Monomers. Polym.* 24 (2021) 330–342, doi:10.1080/15685551.2021.1997178.
- [55] M. Elkabous, M. Ouachekradi, C. Sergent, Y. Karzazi, Electron transfer mechanism from D- π -A metal-free organic dyes to TiO₂ surface: A theoretical exploration with insights into new materials, in: M. Boutahir, E. El Mehdi (Eds.), *Advanced Materials for Sustainable Energy and Engineering*, Engineering Materials, Springer, Cham., 2025, doi:10.1007/978-3-031-75032-8_10.

- [56] L. Ma, H. Yao, J. Zhang, Z. Chen, J. Wang, J. Qiao, S. Wang, Z. Bi, Z. Li, X. Hao, Z. Wei, W. Ma, J. Hou, Morphology control by tuning electrostatic interactions for efficient polythiophene-based all-polymer solar cells, *Chem* 9 (2023) 2518–2529, doi:10.1016/j.chempr.2023.04.021.
- [57] A. Slimi, M. Hachi, A. Fitri, A.T. Benjelloun, S. Elkhatabi, M. Benzakour, M. Mcharfi, M. Khenfouch, I. Zorkani, M. Bouachrine, Effects of electron acceptor groups on triphenylamine-based dyes for dye-sensitized solar cells: Theoretical investigation, *J. Photochem. Photobiol. A* 398 (2020) 112572, doi:10.1016/j.jphotochem.2020.112572.
- [58] G. Deogratias, O.S. Al-Qurashi, N. Wazzan, T. Pogrebnyaya, A. Pogrebnoi, Effect of substituent in the acceptor on optical and electronic properties of triphenylamine based dyes: A density functional theory/time-dependent density functional theory investigation, *Mater. Sci. Semicond. Process* 150 (2022) 106935, doi:10.1016/j.mssp.2022.106935.
- [59] D. Meng, D. Sun, C. Zhong, T. Liu, B. Fan, L. Huo, Y. Li, W. Jiang, H. Choi, T. Kim, J.Y. Kim, Y. Sun, Z. Wang, A.J. Heeger, High-performance solution-processed non-fullerene organic solar cells based on selenophene-containing perylene bisimide acceptor, *J. Am. Chem. Soc.* 138 (2016) 375–380, doi:10.1021/jacs.5b11149.
- [60] S. Böhm, O. Exner, Prediction of molecular dipole moments from bond moments: Testing of the method by DFT calculations on isolated molecules, *Phys. Chem. Chem. Phys* 6 (2004) 510–514, doi:10.1039/b312595p.
- [61] Q. Tao, M. Xiao, M. Zhu, L. Shao, Z. Sui, P. Wang, G. Huang, Y. Pei, W. Zhu, F. Huang, Improving self-assembly behavior and photovoltaic performance of the indacenodithiophene-based small molecules via increasing dipole moment of the terminal group, *Dyes. Pigm.* 144 (2017) 142–150, doi:10.1016/j.dyepig.2017.05.012.
- [62] T. Lu, F. Chen, Multiwfn: A multifunctional wavefunction analyzer, *J. Comput. Chem.* 33 (2012) 580–592, doi:10.1002/jcc.22885.
- [63] T. Le Bahers, C. Adamo, I. Ciofini, A qualitative index of spatial extent in charge-transfer excitations, *J. Chem. Theory. Comput.* 7 (2011) 2498–2506, doi:10.1021/ct200308m.
- [64] C.A. Guido, P. Cortona, B. Mennucci, C. Adamo, On the metric of charge transfer molecular excitations: A simple chemical descriptor, *J. Chem. Theory. Comput.* 9 (2013) 3118–3126, doi:10.1021/ct400337e.
- [65] J.C. Lee, J.D. Chai, S.T. Lin, Assessment of density functional methods for exciton binding energies and related optoelectronic properties, *RSC Adv.* 5 (2015) 101370–101376, doi:10.1039/c5ra20085g.
- [66] T. Wang, G. Kupgan, J.L. Brédas, Organic photovoltaics: Relating chemical structure, local morphology, and electronic properties, *Trends. Chem.* 2 (2020) 535–554, doi:10.1016/j.trechm.2020.03.006.
- [67] O. Guvench, A.D. MacKerell, Comparison of protein force fields for molecular dynamics simulations, *Methods. Mol. Biol.* 443 (2008) 63–88, doi:10.1007/978-1-59745-177-2_4.
- [68] K.M. Katubi, M. Saqib, A. Rehman, S. Murtaza, S. Hussain, Z.A. Alrowaili, M.S. Al-Buriah, Theoretical designing of small molecule donors for organic solar cells: Analyzing the effect of molecular polarity through structural engineering at terminal position, *Chem. Phys. Lett.* 814 (2023) 140349, doi:10.1016/j.cplett.2023.140349.